System Identification for a Small, Rudderless, Fixed-Wing Unmanned Aircraft

Raghu Venkataraman* and Peter Seiler†
University of Minnesota, Minneapolis, Minnesota 55455

This paper presents a system identification procedure for a class of small, rudderless, fixed-wing unmanned aircraft. The procedure is demonstrated on an aircraft that is equipped with only two aerodynamic control surfaces (called elevons) and one electric motor. A physics-based, first-principles approach is used to obtain the initial model parameters. The initial model is used to design flight tests wherein the longitudinal and the lateral-directional dynamics are separately excited. The aircraft is rudderless and this introduces a key challenge in the model identification. Specifically, the lateral-directional model has more free parameters than can be identified using the elevon excitations alone. This paper resorts to two novel steps to navigate this roadblock. First, this paper uses black-box methods to identify sensitive modes whose damping ratios and natural frequencies change significantly compared to their initial values. Second, grey-box methods are used to update the stability and control derivatives related to these sensitive modes, while retaining the remaining derivatives at their respective initial values. Additional flight tests are conducted to validate the updated model parameters.

I. Introduction

SMALL unmanned aircraft systems (UAS) are finding increasingly autonomous roles in various civilian and commercial applications. The development of guidance, navigation, and control algorithms for increased autonomy requires an accurate understanding of the flight dynamics of the aircraft. Modeling and system identification are thus important and relevant tasks in this process. In this paper, first principles are used to build a nonlinear, six degrees-of-freedom model of a small, rudderless, fixed-wing aircraft. Grey-box system identification is then used to improve the estimates of the model parameters.

Several textbooks discuss the process of modeling the flight dynamics of rigid-body aircraft [1, 2] and provide the mathematical background underpinning system identification theory [3, 4]. In addition, several textbooks apply system identification concepts specifically to fixed-wing and rotary-wing aircraft [5]. These include both time-domain and frequency-domain methods [6, 7]. Some papers have proposed novel identification techniques, including real-time identification, and efficient flight test input design [8–10]. Other papers focus on system identification for small

*Graduate Student, Department of Aerospace Engineering and Mechanics; venka085@umn.edu.
†Associate Professor, Department of Aerospace Engineering and Mechanics; seile017@umn.edu.

unmanned aircraft, including helicopter [11, 12], fixed-wing [13–16], and multicopter [17] platforms. Software tools are also available to automate the aircraft system identification process [5, 18].

This paper focuses on the modeling and system identification of small, rudderless, fixed-wing UAS. Such UAS have become increasingly popular over the last decade for aerial photography and mapping applications. Some examples include the Agribotix Hornet, Trimble UX5, senseFly eBee, RoboFlight RF1, and Sentera Vireo. The lack of a rudder is a consequence of the size, weight, and power constraints imposed by their small form factor. All of the above examples feature only a pair of aerodynamic control surfaces (called elevons) and one electric motor. In contrast to conventional fixed-wing UAS, the literature on modeling the flight dynamics of rudderless, fixed-wing UAS is sparse. One approach is to use potential flow-based solvers and wind tunnel tests [19]. Another approach relies on system identification flight experiments, as explained next.

Identifying the longitudinal dynamics of this class of UAS is relatively straightforward since the short period and phugoid modes are weakly coupled (as is the case for most rigid, fixed-wing aircraft). Consequently, the aerodynamic parameters affecting each mode may be identified independent of the other using separate reduced-order models. The lateral-directional modes, on other hand, are strongly coupled. For most conventional fixed-wing UAS, the aerodynamic parameters affecting these modes are identified simultaneously using aileron and rudder excitations (e.g., see [14]). However, for rudderless, fixed-wing UAS, there are too many free aerodynamic parameters in the lateral-directional model that all of them cannot be identified using the aileron excitations. This problem has received little attention in the literature. Among the papers that do consider the system identification of small, rudderless, fixed-wing UAS, some only identify black-box input-output models [20, 21] whereas others also identify the underlying aerodynamic stability and control derivatives [22].

While this paper shares the same system identification objectives as [22], it follows a novel two-step approach to identify the stability and control derivatives. In particular, given an initial model of the aircraft dynamics, this paper first uses black-box models to identify sensitive (poorly modeled) modes whose damping ratios and natural frequencies change significantly compared to their initial values. This knowledge is then exploited within grey-box models to selectively update the stability and control derivatives related to these sensitive modes, while retaining the remaining derivatives at their respective initial values. For example, Section III.C demonstrates that because the initial model accurately describes the roll subsidence mode, there is no need to update the derivatives that affect it. In contrast, all the stability and control derivatives are updated through a direct one-step fit of the lateral-directional state-space model in [22]. This one-step approach over-parameterizes the model. The novel two-step method proposed in this paper focuses on the identification of the most uncertain lateral-directional stability derivatives. In addition, the methods presented in [22] require measurements of the roll rate, yaw rate, lateral acceleration, and reconstructed side acceleration. In contrast, the method proposed in this paper only requires the roll rate measurement to identify the lateral-directional dynamics. Thus it is widely applicable to low-cost, rudderless, fixed-wing UAS that are often equipped with a minimal sensor set.

The paper is organized as follows. Section II introduces the rudderless UAS considered in this paper and presents the model structures used in the system identification. Section III describes the design of the flight experiments and presents the results of the lateral-directional system identification. Section IV validates the identified models and Section V presents the conclusions. SI units $(\mathrm{m}, \mathrm{kg}, \mathrm{s})$ are used for all the signals in the aircraft model. All angular quantities are expressed in radians.

II. Preliminaries

A. Rudderless Unmanned Aircraft

This paper considers the aircraft shown in Fig. 1 as an example to describe the system identification procedure. This aircraft was originally built by Sentera, LLC and is currently maintained and operated by the University of Minnesota. The fully integrated aircraft has a gross mass of 1.28 kg, a wing span of 0.97 m, and a fuselage length of 0.52 m. It is equipped with a pair of independently actuated elevons and a puller-type electric motor that drives a fixed-pitch propeller. Sensing is provided via an inertial measurement unit, a global positioning system receiver, a magnetometer, and a pitot-static system. A flight computer implements the software for sensing, navigation, guidance, control, telemetry, and data logging [23].

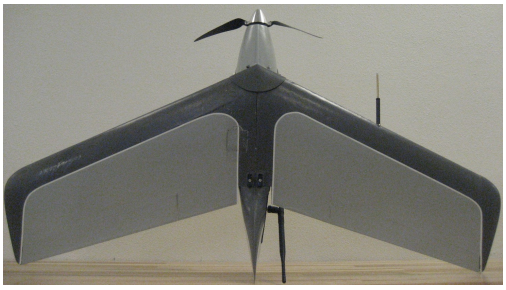

Fig. 1 The Sentera Vireo – the small, rudderless, fixed-wing UAS considered in this paper.

A nonlinear, six degrees-of-freedom model of this aircraft is developed using physics-based first-principles [23]. In particular, the geometric and inertial properties of this aircraft are modeled using computer-aided drawings. The propulsive forces are modeled using wind tunnel experiments. The aerodynamic characteristics (stability and control derivatives) are initially estimated using the vortex lattice method (VLM), using the Athena Vortex Lattice (AVL) software [24]. Additional details on this first-principles modeling can be found in [23]. Since this aircraft is assumed to be rigid, the pertinent states are the Euler angles (ϕ, θ, ψ), the angular velocity in the body axes (p, q, r), the airspeed in the body axes (u, v, w), and the position of the aircraft in a local North-East-Down frame (p_N, p_E, p_D). The nonlinear equations of motion of rigid, fixed-wing aircraft are documented in textbooks [1, 2] and are thus not repeated here.

The throttle δ_t is normalized to the interval $[0, 1]$. The left δ_l and the right δ_r elevons each have a deflection range of $[-30, +20]\,^\circ$, where positive values correspond to trailing-edge down deflections. As such, each elevon excites both the

longitudinal and the lateral-directional dynamics. Therefore, for modeling convenience, these dynamics are decoupled by expressing the elevons in terms of the traditional elevator δ_e and the aileron δ_a via the relations $\delta_l = \delta_e - \delta_a$ and $\delta_r = \delta_e + \delta_a$. The virtual inputs δ_e and δ_a are assumed to affect only the longitudinal and the lateral-directional dynamics, respectively. The dynamics of the throttle and the elevon actuators are respectively given by:

$$G_t(s) = \frac{\omega_t}{s + \omega_t} \quad \text{and} \quad G_a(s) = \frac{\omega_a^2}{s^2 + 2\zeta_a\omega_a s + \omega_a^2}, \tag{1}$$

where the model parameters are experimentally estimated [23] as: $\omega_t = 6.28\ \text{rad}\,\text{s}^{-1}$, $\zeta_a = 0.77$, and $\omega_a = 62.8\ \text{rad}\,\text{s}^{-1}$.

Since VLM assumes potential flow, the initial model has inaccurate stability and control derivatives. The system identification focuses on finding more accurate estimates of these derivatives. At a fixed airspeed, the flight dynamics are assumed to be linear time-invariant (LTI). The flight tests are conducted at a mean airspeed of $19\ \text{m}\,\text{s}^{-1}$. The next two sections present parametrized transfer function ("black-box") and state-space ("grey-box") forms of the LTI dynamics for system identification. The principles of flight dynamics [1, 2] inform the parametrization of the black-box and the grey-box LTI models. For example, the grey-box LTI models are parametrized by *dimensional* stability and control derivatives (see Table 4.2 and Table 5.1 in [2]). The unknown parameters are generically denoted by Θ.

B. Longitudinal Model

The longitudinal dynamics are affected by the inputs δ_t and δ_e. Since a propulsion model is already developed using experimental data [23], the system identification focuses on the pitch rate response to the elevator input. In particular, the longitudinal dynamics are composed of the short-period and the phugoid modes, which contribute a total of four poles. In addition, the pitch rate output is associated with three zeros, including a zero on the imaginary axis [1]. Thus, the elevator-to-pitch rate response is described by the black-box model [1]:

$$G_{lon}(s,\Theta) = \frac{q(s)}{\delta_e(s)} = \frac{k_q s\left(s + z_{\theta_1}\right)\left(s + z_{\theta_2}\right)}{\left(s^2 + 2\zeta_p\omega_p s + \omega_p^2\right)\left(s^2 + 2\zeta_s\omega_s s + \omega_s^2\right)}, \tag{2}$$

where the denominator is expressed in terms of the damping ratio ζ and the natural frequency ω of the phugoid and the short period modes and the numerator is expressed in terms of the gain k_q and the zeros z_{θ_1} and z_{θ_2}.

The equivalent grey-box LTI model in the time-domain is given by [2]:

$$\dot{x}_{lon} = A_{lon}(\Theta)\, x_{lon} + B_{lon}(\Theta)\, \delta_e, \tag{3}$$

where the state is $x_{lon} = [u, w, q, \theta]^T$ and the matrices are:

$$A_{lon}(\Theta) = \begin{bmatrix} X_u & X_w & X_q - \bar{w} & -g\cos\bar{\theta} \\ Z_u & Z_w & Z_q + \bar{u} & -g\sin\bar{\theta} \\ M_u & M_w & M_q & 0 \\ 0 & 0 & 1 & 0 \end{bmatrix} \quad \text{and} \quad B_{lon}(\Theta) = \begin{bmatrix} X_{\delta_e} \\ Z_{\delta_e} \\ M_{\delta_e} \\ 0 \end{bmatrix}. \tag{4}$$

The A_{lon} and B_{lon} matrices are populated with the dimensional stability and control derivatives, the trim variables $\bar{u}$, $\bar{w}$, and $\bar{\theta}$, and the acceleration due to gravity g. The output equation, which is not shown, simply picks q from the state x_{lon}.

At an airspeed of 19 m s^{-1}, the *initial* elevator-to-pitch rate black-box model, with data obtained via VLM and ground-based experiments, is:

$$G_{lon}(s) = \frac{q(s)}{\delta_e(s)} = \frac{-279.22\, s\,(s + 0.3778)(s + 4.943)}{(s^2 + 0.267s + 0.4964)(s^2 + 13.59s + 292.3)} \tag{5}$$

and the populated matrices of the corresponding grey-box LTI model are:

$$A_{lon} = \begin{bmatrix} -0.2714 & 0.4718 & -0.2857 & -9.804 \\ -0.9315 & -6.963 & 17.1 & -0.1417 \\ 0.208 & -14.39 & -6.621 & 0 \\ 0 & 0 & 1 & 0 \end{bmatrix} \quad \text{and} \quad B_{lon} = \begin{bmatrix} -0.8428 \\ -37.13 \\ -279.2 \\ 0 \end{bmatrix} \tag{6}$$

Figure 2 shows the Bode diagram of $G_{lon}G_a$, i.e. the response from the elevator command δ_{ec} to the pitch rate q. The markers indicate the natural frequencies of longitudinal modes and the actuator. The highlighted portion indicates the frequency range covered by the input excitation (as explained further below).

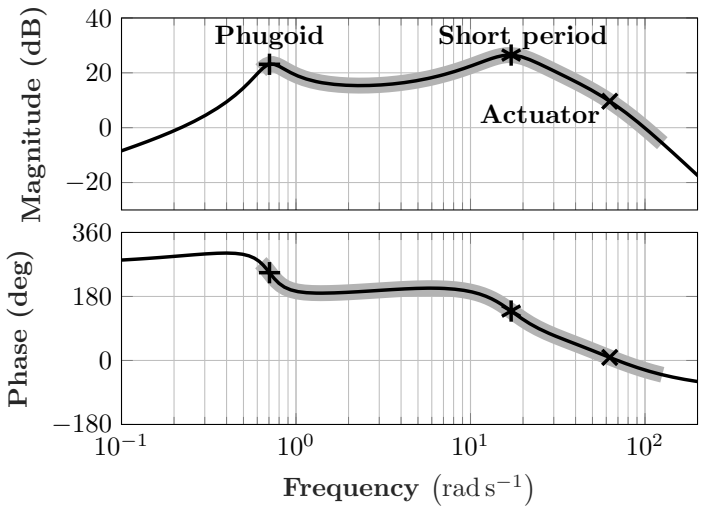

Fig. 2 The Bode diagram of the initial model from the elevator command δ_{ec} to the pitch rate q.

C. Lateral-Directional Model

The system identification for the lateral-directional dynamics focuses on the roll rate response to aileron input. In particular, the lateral-directional dynamics are composed of the roll subsidence, the spiral, and the dutch roll modes, which contribute a total of four poles. In addition, the roll rate output is associated with three zeros, including a zero on the imaginary axis [1]. Thus, the aileron-to-roll rate response is described by the black-box model [1]:

$$G_{lat}(s, \Theta) = \frac{p(s)}{\delta_a(s)} = \frac{k_p s \left(s^2 + 2\zeta_\phi \omega_\phi s + \omega_\phi^2\right)}{\left(s + T_s^{-1}\right)\left(s + T_r^{-1}\right)\left(s^2 + 2\zeta_d \omega_d s + \omega_d^2\right)}, \tag{7}$$

where the denominator is expressed in terms of the damping ratio ζ_d and the natural frequency ω_d of the dutch roll mode and the time constants of the spiral and the roll subsidence modes. The numerator is expressed in terms of the gain k_p and parameters ζ_ϕ and ω_ϕ.

The equivalent grey-box LTI model in the time-domain is given by [2]:

$$M_{lat}\,\dot{x}_{lat} = \bar{A}_{lat}\,(\Theta)\,x_{lat} + \bar{B}_{lat}\,(\Theta)\,\delta_a, \tag{8}$$

where the state is $x_{lat} = [v, p, r, \phi]^T$ and the matrices are:

$$M_{lat} = \begin{bmatrix} 1 & 0 & 0 & 0 \\ 0 & 1 & -\frac{I_{xz}}{I_{xx}} & 0 \\ 0 & -\frac{I_{xz}}{I_{zz}} & 1 & 0 \\ 0 & 0 & 0 & 1 \end{bmatrix}, \quad \bar{A}_{lat}\,(\Theta) = \begin{bmatrix} Y_v & Y_p+\bar{w} & Y_r-\bar{u} & g\cos\bar{\theta} \\ L_v & L_p & L_r & 0 \\ N_v & N_p & N_r & 0 \\ 0 & 1 & \tan\bar{\theta} & 0 \end{bmatrix}, \quad \text{and} \quad \bar{B}_{lat}\,(\Theta) = \begin{bmatrix} Y_{\delta_a} \\ L_{\delta_a} \\ N_{\delta_a} \\ 0 \end{bmatrix}. \tag{9}$$

The M_{lat} matrix is populated with the moments and product of inertia terms. The $\bar{A}_{lat}$ and $\bar{B}_{lat}$ matrices are populated with the dimensional stability and control derivatives, the trim variables $\bar{u}$, $\bar{w}$, and $\bar{\theta}$, and the acceleration due to gravity g. The output equation, which is not shown, simply picks p from the state x_{lat}.

At an airspeed of 19 $\mathrm{m\,s^{-1}}$, the *initial* aileron-to-roll rate black-box model, with data obtained via VLM and ground-based experiments, is:

$$G_{lat}\,(s) = \frac{p\,(s)}{\delta_a\,(s)} = \frac{-427.3(s - 0.007428)(s^2 + 1.467s + 38.58)}{(s + 14.63)(s + 0.004129)(s^2 + 0.8025s + 48.77)} \tag{10}$$

and the populated matrices of the corresponding grey-box LTI model are:

$$M_{lat} = \begin{bmatrix} 1 & 0 & 0 & 0 \\ 0 & 1 & -0.0801 & 0 \\ 0 & -0.0471 & 1 & 0 \\ 0 & 0 & 0 & 1 \end{bmatrix}, \quad \bar{A}_{lat} = \begin{bmatrix} -0.5175 & 0.3562 & -18.83 & 9.804 \\ -5.984 & -14.03 & 2.424 & 0 \\ 1.855 & -1.39 & -0.8849 & 0 \\ 0 & 1 & 0.01445 & 0 \end{bmatrix} \quad \text{and} \quad \bar{B}_{lat} = \begin{bmatrix} -0.7391 \\ -427.3 \\ -11.92 \\ 0 \end{bmatrix}. \tag{11}$$

The numerators in Equations (7) and (10) are slightly different because the former is obtained analytically whereas the latter is obtained numerically. In particular, Equation (7) is obtained by analytically linearizing the equations of motion, which results in a zero that is located exactly on the imaginary axis. On the other hand, errors in the numerical trim and linearization that is used to obtain Equation (10) cause the zero to be slightly perturbed from the imaginary axis.

Figure 3 shows the Bode diagram of $G_{lat}G_a$, i.e. the response from the aileron command δ_{ac} to the roll rate p. The markers indicate the natural frequencies of the lateral-directional modes and the actuator. The spiral mode lies outside the axis limits. The highlighted portion of the diagram indicates the frequency range covered by the input excitation.

III. System Identification

A. Design of Flight Experiments

The system identification process aims to experimentally estimate the parameters of the black-box and the grey-box LTI models. The pilot sets up the aircraft to fly at the trim airspeed, at constant altitude, and along a constant course.

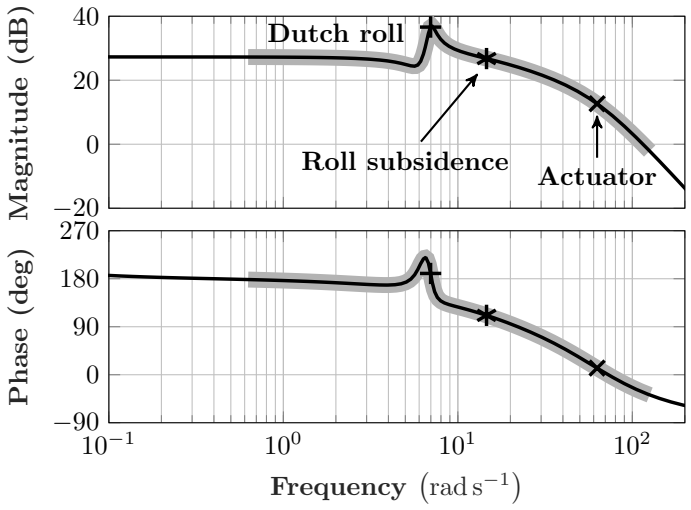

Fig. 3 The Bode diagram of the initial model from the aileron command δ_{ac} to the roll rate p.

The experiments are conducted open-loop to simplify the analysis. In order to satisfy the assumption of local linearity, it is important that the airspeed of the aircraft stay more or less constant throughout the experiment. The pilot compensates for the disturbing effects of wind gusts and turbulence and, thus, functions as a low-bandwidth controller. The system identification focuses on experimentally characterizing the elevator-to-pitch rate and the aileron-to-roll rate aircraft responses. The Bode diagrams (Fig. 2 and Fig. 3) guide the design of the experiments. The elevator and the aileron commands are specified using the chirp function $A\cos\left(\omega_i\left(t\right)t\right)$, where A and $\omega_i\left(t\right)$ denote the amplitude and the instantaneous frequency, respectively. The instantaneous frequency is swept linearly over time as $\omega_i\left(t\right) = \omega_1 + \frac{(\omega_2-\omega_1)}{2T_{ch}}t$, where ω_1, ω_2, and T_{ch} denote the start frequency, the end frequency, and the sweep duration, respectively.

Chirps commands can be designed to cover a wide frequency range and have yielded excellent results in the past [14, 15]. The spectral content of δ_{ec} and δ_{ac} are designed to span the longitudinal and lateral-directional modes, respectively. However, the frequency range of the chirp is dictated by practical considerations. For instance, 20 s is the longest duration that the aircraft can fly along a constant course and remain within the airspace available at the test site. This sets a lower bound on the chirp frequencies. In addition, the median sample rate of the flight computer is 90 Hz $\left(566\ \mathrm{rad\,s^{-1}}\right)$. Thus, the Nyquist frequency of 283 $\mathrm{rad\,s^{-1}}$ is an upper bound on the chirp frequencies for achieving alias-free sampling. Table 1 summarizes the natural frequencies of the aircraft dynamic modes, the actuator bandwidth, and the bounds on the chirp frequency. Given these considerations, the final chirp commands are designed to span the frequency range $[0.63, 126]$ $\mathrm{rad\,s^{-1}}$. This range is highlighted in the Bode diagrams shown in Fig. 2 and Fig. 3, and includes the natural frequencies of all longitudinal and lateral-directional modes, as well as the actuator bandwidth.

Since the $[0.63, 126]$ $\mathrm{rad\,s^{-1}}$ frequency range is too wide to be completed within 20 s, it is divided into three smaller segments (Table 2). In particular, the low, the medium, and the high segments use overlapping frequency ranges

Table 1 Key flight dynamic modes and limiting frequencies.

Mode/bound	Frequency $\left(\text{rad}\,\text{s}^{-1}\right)$	Source
Phugoid mode	0.7	Initial LTI model
Dutch roll mode	7	Initial LTI model
Roll subsidence mode	14.6	Initial LTI model
Short period mode	17	Initial LTI model
Time delay	20	Computed as 0.05 s (Section III.D)
Actuator bandwidth	57	Benchtop experiment [23]
Nyquist frequency	283	One-half of the sample rate
Median sample rate	566	Firmware limitation [23]

and correspond to 30, 20, and 10-fold increases between the start and end frequencies, respectively. Each segment is assigned a chirp ID, as shown in Table 2. Two flights are conducted for the system identification. The first flight commands elevator chirps over 20 s and uses the pitch rate response to identify the longitudinal dynamics. The second flight commands aileron chirps over 15 s and uses the roll rate response to identify the lateral-directional dynamics.

Table 2 The chirp parameters used in the flight experiments.

Range	Chirp ID	Amplitude	Frequency	Increase	Trials
Low	Ch1	2°	$[0.63, 18.9]$ rad s^{-1}	30-fold	3
Medium	Ch2	2°	$[3.14, 62.8]$ rad s^{-1}	20-fold	3
High	Ch3	2°	$[12.6, 126]$ rad s^{-1}	10-fold	1

Multiple trials are conducted to obtain a large sample size. The amplitude of the chirp command is set equal to 2° across all the experiments. Prior flight tests helped determine that this amplitude yields a sufficiently high signal-to-noise ratio (SNR) in the pitch and the roll rate signals, while keeping deviations from the trim point small. Even with the 2° chirp amplitude, the aircraft deviates from its trim point due to wind gusts and turbulence. The pilot corrects for these deviations using the RC transmitter. The flight computer superimposes the pilot stick inputs over the chirp commands. Thus, the system identification considers the input as the total elevator or aileron command.

B. Prediction Error Minimization

This paper identifies the model parameters using the prediction error minimization (PEM) method [3]. Let $y\left(t_j\right) \in \mathbb{R}^{n_y}$ and $\hat{y}\left(t_j|\Theta\right) \in \mathbb{R}^{n_y}$ denote the measured and the model-predicted outputs at the j^{th} sample time. The prediction error is defined as: $e\left(t_j|\Theta\right) = y\left(t_j\right) - \hat{y}\left(t_j|\Theta\right)$. If the experiment contains a total of N data samples, the prediction error is computed at each sampling instant t_j, thereby resulting in the error sequence $\{e\left(t_j|\Theta\right)\}_1^N$. In general, $\{e\left(t_j|\Theta\right)\}_1^N$ is filtered through a user-specified, stable, linear filter. The goal is then to minimize the filtered prediction error sequence $\{\bar{e}\left(t_j|\Theta\right)\}_1^N$, where the overline distinguishes it from the unfiltered sequence. The size of this sequence

can, in general, be measured using any vector norm. This paper uses the quadratic norm and results in the cost function:

$$V(\Theta) = \frac{1}{N}\sum_{j=1}^{N} \bar{e}\left(t_j|\Theta\right)^T \bar{e}\left(t_j|\Theta\right). \tag{12}$$

The objective of PEM is to minimize $V(\Theta)$ over the set of parameters. The optimal estimate is denoted by $\hat{\Theta}$. Various model quality metrics exist in the literature to evaluate the quality of the identified model (see Section 16.4 in [3]). This paper uses the *fit percent*, which is denoted by η and is defined as:

$$\eta = 100 \cdot \left(1 - \frac{\left\|E\left(\hat{\Theta}\right)\right\|_F}{\left\|Y - \bar{Y}\,\mathbf{1}^T\right\|_F}\right), \tag{13}$$

where, $E\left(\hat{\Theta}\right) = \left[\bar{e}\left(t_1|\hat{\Theta}\right), \ldots, \bar{e}\left(t_N|\hat{\Theta}\right)\right]$ and $Y = [y(t_1), \ldots, y(t_N)]$ are matrices in $\mathbb{R}^{n_y \times N}$ formed from the filtered prediction error $\{\bar{e}\left(t_j|\hat{\Theta}\right)\}_1^N$ and output $\{y\left(t_j\right)\}_1^N$ sequences, respectively. Moreover, $\bar{Y}$ is a vector in $\mathbb{R}^{n_y}$ that is formed by computing the mean of each row of Y, $\mathbf{1}$ is a column vector of ones such that the product $\bar{Y}\,\mathbf{1}^T$ is a matrix in $\mathbb{R}^{n_y \times N}$, and $\|\cdot\|_F$ denotes the Frobenius norm in Equation (13). The value of η varies between $-\infty$ (bad fit) and 100 (perfect fit). If $\eta = 0$, then the model fits the data no better than the sample mean of the output.

The longitudinal model identification uses the elevator-to-pitch rate response of the aircraft to identify the short period mode. Since it is fairly straightforward, the reader is referred to [23] for its details. The challenge lies in the lateral-directional model identification, as explained next.

C. Lateral-Directional Model Identification

1. Summary of experiments

Seven experiments are performed by commanding aileron chirps using the parameters shown in Table 2. The experiments are labeled using the nomenclature SA-Ch**X**-T**Y**, where **X** denotes the chirp ID number and **Y** denotes the trial number. For illustrative purposes, Fig. 4 shows the aileron chirp command and the corresponding roll rate response observed during the experiment SA-Ch2-T1. In this experiment, the chirp spans the medium frequency range $[3.14, 62.8]$ rad s^{-1} and thus excites the dutch roll and the roll subsidence modes. This is visible in the plot of the roll rate, whose magnitude rolls off midway through the chirp. In addition, the low frequency pilot stick inputs, and the small aileron trim setting, are visible in the plot of the aileron command. The time history plots of the other aileron chirp experiments appear similar to Fig. 4, and are not shown here for brevity.

The spiral mode lies outside the frequency range of all the chirp commands and is not observed during any of the experiments. On the other hand, the roll subsidence mode frequency of 14.6 rad s^{-1} lies within the span of all the chirp commands and the dutch roll mode frequency of 7 rad s^{-1} lies within the spans of the Ch1 and Ch2 chirp commands. Ideally, the identification would only focus on the dutch roll and the roll subsidence modes. However, unlike the longitudinal case, a clean separation between the lateral-directional modes is difficult to achieve. Reduced order

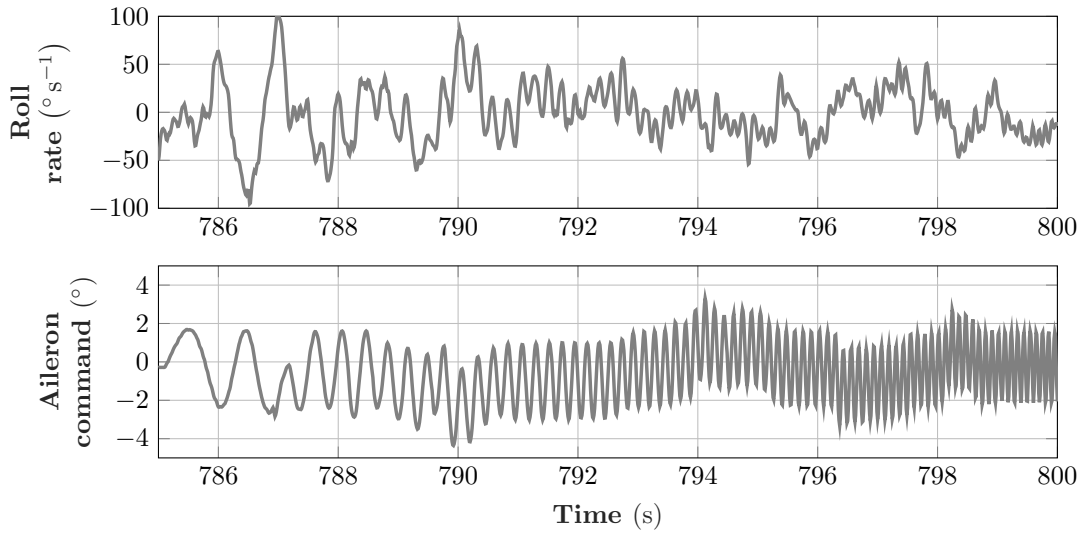

Fig. 4 The aileron chirp command and the roll rate response during the experiment SA-Ch2-T1.

models for the lateral-directional modal dynamics are generally insufficiently accurate to be of any real use [1]. Hence, the black-box model identification necessarily considers all the lateral-directional modes. However, as will be seen shortly, the grey-box model structure offers some latitude in targeting specific modes during the identification.

The coherency spectrum between p and δ_{ac} [3] is computed for each of the seven chirp experiments and displayed in Fig. 5. These spectra guide the selection of the experiments for the system identification by highlighting the frequency ranges where the coherency is high. Based on the coherencies attained at the natural frequencies of the dutch roll and the roll subsidence modes, the experiment SA-Ch2-T1 is selected for the system identification. The experiment SA-Ch3-T1 is not included because the dutch roll mode lies outside its frequency range. The selected experiment is detrended, by removing the sample mean (see Chapter 14 in [3]).

2. Frequency response function and black-box model

The frequency response function relating p and δ_{ac} is computed [3]. This function not only characterizes the dynamics of the aircraft G_{lat} and the actuator G_a, but also captures the time delay τ_f. The flight data is used to estimate τ_f as 0.05 s (see Section III.D for details). Further, since the actuator model is obtained from benchtop experiments [23], the system identification problem reduces to characterizing G_{lat}. The parameters of the black-box model (Equation (7)) are estimated using PEM. Since the lateral-directional modes cannot be separated, all the parameters shown in Equation (7) are estimated from the selected experiment. PEM results in a spiral mode time constant of 2.5 s, a roll subsidence mode time constant of 0.078 s, and a dutch roll mode damping ratio of 0.12 and natural frequency of 4.8 rad s^{-1}. The corresponding fit percent is 80%.

The modal parameters of the black-box model are different from those of the initial model. In particular, the dutch

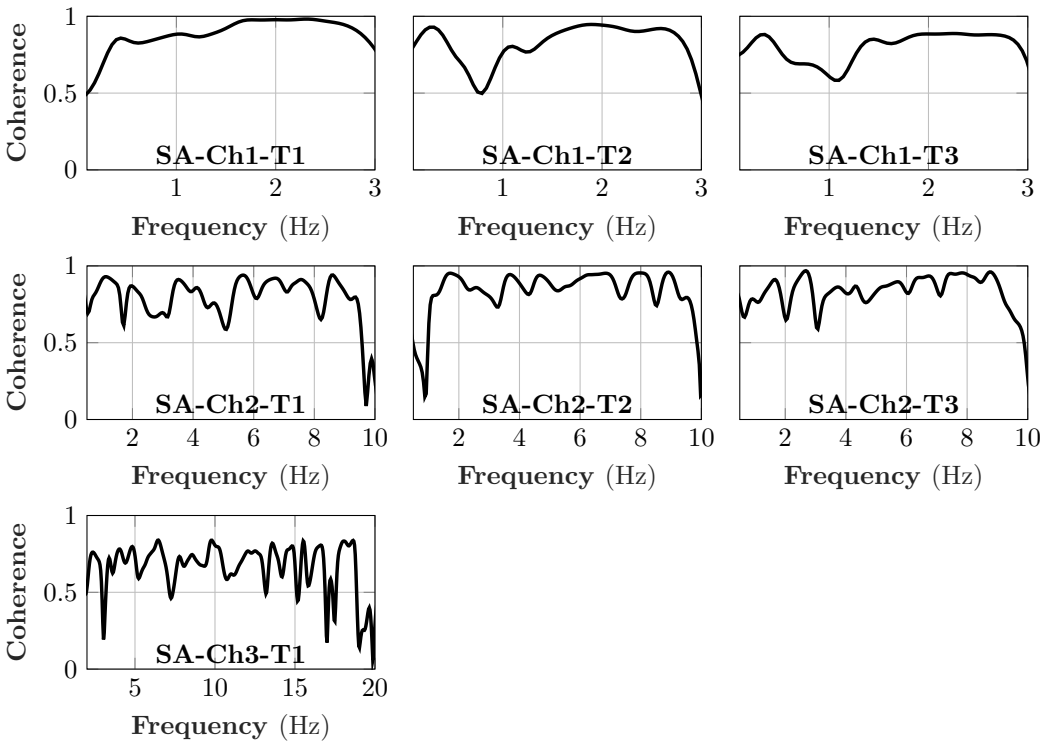

Fig. 5 The coherency spectra obtained for the seven aileron chirp experiments.

roll mode damping ratio increases from 0.06 to 0.12 and the natural frequency decreases from 7 rad s^{-1} to 4.8 rad s^{-1}. The time constant of the roll subsidence mode slightly increases from 0.07 s to 0.078 s. The estimated spiral mode time constant of 2.5 s is two orders of magnitude lower than the initial value of 242 s. Since the spiral mode is not excited during any of the experiments, this estimate is inaccurate and does not correspond to any physical mode.

Figure 6 plots the Bode diagrams of the frequency response function, the black-box model, and the initial model from the aileron command δ_{ac} to the roll rate p. The Bode diagrams capture the dutch roll and roll subsidence modes and the actuator dynamics. The rapid phase loss that is seen in all of the plots is attributed to the time delay of 0.05 s. The fit percent of 80% implies that the identified black-box model accurately describes the frequency response function, and hence the actual lateral-directional aircraft dynamics, in the frequency range $[3.14, 62.8]$ rad s^{-1}. However, as seen in Fig. 6, the initial model poorly describes the frequency response function at all frequencies and is insufficient for the purpose of control design. While the black-box model correctly describes the lateral-directional dynamics, it cannot be used to update the initial model parameters. Hence, the next section presents the grey-box parameter estimation.

3. Grey-box model

Equations (8) and (9) describe the grey-box LTI model for the lateral-directional aircraft dynamics. Since this model is parametrized using the dimensional stability and control derivatives, it relates back to the aerodynamic model.

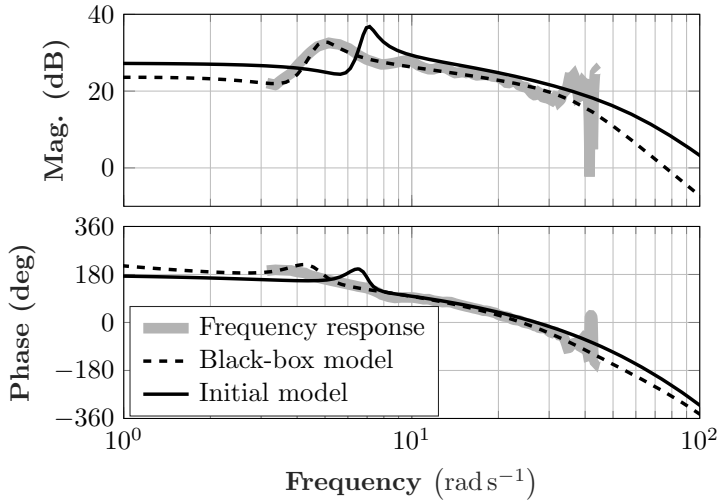

Fig. 6 The frequency response function, the black-box model, and the initial model from the aileron command δ_{ac} to the roll rate p.

Additionally, the grey-box model structure offers greater latitude in targeting specific modes, via the dimensional stability and control derivatives, as compared to the black-box model structure. In particular, each lateral-directional mode is predominantly affected by a subset of the dimensional stability derivatives [1], as shown in Table 3. The derivative Y_p, which captures the side force produced due to the roll rate, is small for the Vireo and thus does not appear in Table 3.

Table 3 Each lateral-directional mode is predominantly affected by a subset of the stability derivatives.

Mode	Stability derivative
Spiral	L_v, L_r, N_v, N_r
Dutch roll	Y_v, Y_r, N_v, N_r
Roll subsidence	L_p, N_p

The goal of the grey-box parameter estimation is to update some of these derivatives, such that the updated model adequately describes the frequency response function shown in Fig. 6. Table 3 thus acts as a guide to selecting the parameters to be updated. In this regard, reconsider the results of the black-box parameter estimation. The time constant of the roll subsidence mode increased only slightly from 0.07 s to 0.078 s. Since this mode is already accurately described by the initial model, L_p and N_p are *not* updated. On the other hand, the dutch roll mode damping ratio doubled from 0.06 to 0.12 and the natural frequency decreased from 7 $\mathrm{rad\,s^{-1}}$ to 4.8 $\mathrm{rad\,s^{-1}}$. Since these are significant changes, Y_v, Y_r, N_v and N_r are updated in the grey-box model.

In addition, although the spiral mode is not excited during any of the experiments, Table 3 indicates that the spiral and the dutch roll modes share the N_v and N_r derivatives in common. Updating only some of the derivatives of the spiral mode, and not others, would lead to an over constrained model. Hence, L_v and L_r are also updated. Further,

although the derivative Y_p does not predominantly affect any of the modes, it is updated in order to find the best value that explains the input-output data. Finally, the control derivative L_{δ_a}, which captures the aileron control effectiveness, is also updated since it directly affects the aileron-to-roll rate response.

The eight parameters to be updated are $\Theta = \left[Y_v, Y_p, Y_r, L_v, L_r, N_v, N_r, L_{\delta_a}\right]^T$ and are initialized using VLM. In order to constrain the optimization, each positive parameter in Θ is lower bounded by one-half of its initial value and upper bounded by twice its initial value. This bounding strategy is reversed for negative parameters. These bounds effectively constrain the parameter vector to a hyper-rectangle in $\mathbb{R}^8$. The prediction error minimization method is used to estimate the optimal parameter vector $\hat{\Theta}$ from the experiment SA-Ch2-T1. Table 4 lists the initial and the final values, as well as the lower and the upper bounds, of the parameters of the grey-box model.

Table 4 The initial and updated parameters of the grey-box lateral-directional model.

Derivative	Initial value	Lower bound	Upper bound	Final value
L_{δ_a}	−467.9	−935.9	−234.0	−331.7
L_p	−14.79	not updated		−14.79
L_r	2.604	1.302	5.209	3.160
L_v	−8.960	−17.92	−4.480	−4.849
N_{δ_a}	12.99	not updated		12.99
N_p	−0.646	not updated		−0.646
N_r	−1.079	−2.157	−0.5393	−1.510
N_v	1.387	0.6935	2.774	0.7884
Y_{δ_a}	−0.8474	not updated		−0.8474
Y_p	0.0904	0.0452	0.1807	0.0452
Y_r	0.1892	0.0946	0.3784	0.0946
Y_v	−0.5729	−1.146	−0.2865	−0.7817

Table 4 shows that, among the parameters that are updated, only Y_p and Y_r reach their respective lower bounds at $\hat{\Theta}$. In addition, no parameter reaches its upper bound. By considering the change in the absolute value of each parameter, it is evident that VLM overestimates L_{δ_a}, L_v, N_v, Y_p, and Y_r and underestimates L_r, N_r, and Y_v. The final values of these parameters correspond to a spiral mode time constant of 14 s, a roll subsidence mode time constant of 0.065 s, and a dutch roll mode damping ratio of 0.16 and natural frequency of 4.8 rad s^{-1}. The grey-box parameter estimation achieves a fit percent of 70%, which is 10 percentage points lower than that achieved with the black-box model. This drop in accuracy is expected because the grey-box model structure imposes a greater number of constraints, via the parameters that are not updated, as compared to the black-box model structure.

The modal parameters of the grey-box model are similar to those of the black-box model. Although the derivatives associated with the roll subsidence mode are not updated, its time constant still changes slightly. This shows that, in general, each mode is affected by all the derivatives, and that Table 3 only provides an approximate separation. Further,

the dutch roll mode parameters are very similar between the grey-box and the black-box models. The grey-box spiral mode time constant of 14 s is an order of magnitude lower than the initial value of 242 s. This estimate still cannot be trusted since the spiral mode is not excited during any of the experiments. However, a large uncertainty in the spiral mode time constant is usually not an issue, since the mode is stabilized even by low bandwidth controllers.

Figure 7 plots the Bode diagrams of the frequency response function, the grey-box model, and the initial model from the aileron command δ_{ac} to the roll rate p. The most important observation is that the grey-box model accurately describes the frequency response function, and hence the actual lateral-directional aircraft dynamics, in the frequency range $[3.14, 62.8]$ rad s^{-1}. Further, the dutch roll mode and the actuator bandwidth are visible in the Bode diagrams.

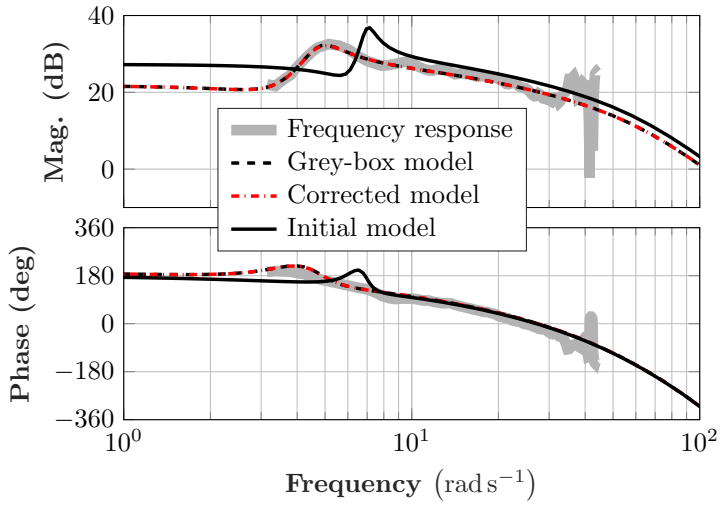

Fig. 7 The frequency response function, the grey-box model, and the initial model from the aileron command δ_{ac} to the roll rate p.

Figure 7 indicates that the grey-box model is sufficient for the purpose of control design. Hence, the final parameter values, shown in Table 4, are used to update the nonlinear aircraft model. After these updates, the nonlinear aircraft model is again linearized at an airspeed of 19 m s^{-1}. The Bode diagram of this so-called *corrected model* is also plotted in Fig. 7. As seen in the figure, there is no distinguishable difference between the corrected model and the grey-box model. This implies that the identified parameters are properly integrated into the nonlinear aircraft model.

D. Time-Delay Estimation

The time delay τ_f is estimated by fitting black-box models with different, but known, fixed delays to the experimental data and observing the resulting fit percent. A simple one-dimensional grid search then yields the time delay, via the corresponding model, that results in the largest fit percent. However, the fit percent is an effective metric only if it strongly depends on the time delay. Practically, this boils down to ensuring that the estimation includes the experiment(s) with the highest frequency content. This is because, for any given signal, the phase loss produced by the time delay

is directly proportional to the frequency of the signal. For the experiments that are described in Section III.A, this is simply achieved by including the high frequency chirp commands (see Table 2). In addition, the effect of the time delay is more pronounced on the highest frequency mode of the system. Since the short period mode is the highest frequency mode of the Vireo, the time delay is estimated using the elevator chirp experiments.

The median sample time during the elevator chirp experiments is $T_s = 0.011$s. Nine different time delays $\tau_f = \{kT_s\}_{k=1}^{9}$ are selected to construct the one-dimensional grid. For each value of τ_f in this grid, a black-box model is identified from δ_{ec} to q. The identification is conducted for the experiments SE-Ch1-T1, SE-Ch1-T2, SE-Ch2-T3, and SE-Ch3-T1. Figure 8 shows the resulting fit percents obtained with each black-box model as a function of the time delay. It is evident from the figure that the fit percents corresponding to $\tau_f = 4T_s$ and $\tau_f = 5T_s$ are significantly larger than those obtained using the other time delays. However, since τ_f is the time delay associated with a continuous-time linear model, it is not restricted to be an integer multiple of T_s. If the black-box identification is repeated for $\tau_f = 4.5T_s$, the resulting fit percents are very close to those obtained using $\tau_f = 4T_s$. Thus, in order to be conservative, the final time delay is selected as $\tau_f = 0.05$ s.

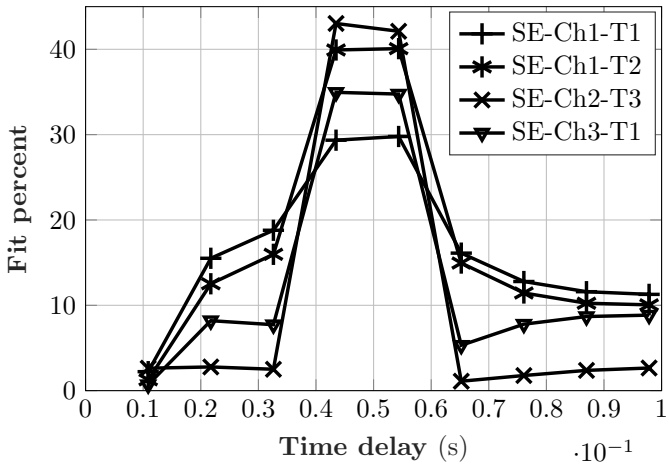

Fig. 8 The time delay is estimated by fitting black-box models with different predetermined delays.

On a related note, if the procedure described above is repeated using the aileron chirp experiments, the resulting fit percents are largely invariant to the time delay. In particular, for each of the SA-Ch**X**-T**Y** experiments, the fit percent varies by less than 4 percentage points across the grid $\tau_f = \{kT_s\}_{k=1}^{6}$ and decreases for larger values of τ_f. This is because the dutch roll mode, with a natural frequency of 4.8 rad s^{-1}, is relatively unaffected by the different amounts of the time delay. Finally, since τ_f is estimated directly from the experimental data, it encompasses delays in the actuators, the flight computer, and the sensors. For simplicity, all of this time delay is grouped at the input to the actuator.

IV. Model Validation

Finally, the identified models are validated using experiments that are not selected during the model identification.

A. Longitudinal Model Validation

Time-domain simulations of the final model are compared against the pitch rate responses recorded during the experiments SE-Ch1-T3, SE-Ch2-T1, and SE-Ch3-T1. This selection includes one trial each from the low, the medium, and the high frequency ranges. None of these experiments, except for SE-Ch3-T1, are selected during the identification. Figure 9 shows the results of the validation over three subplots. The elevator chirp commands span the low (top subplot), the medium (middle subplot), and the high (bottom subplot) frequency ranges. In each subplot, the legend indicates the corresponding fit percent achieved by the final model. The plots indicate that the fit percents progressively decrease from the low to the high frequency ranges. In addition, the fit percent achieved with the experiment SE-Ch1-T3 is approximately 5 percentage points lower than the fit percent achieved during the black-box model identification.

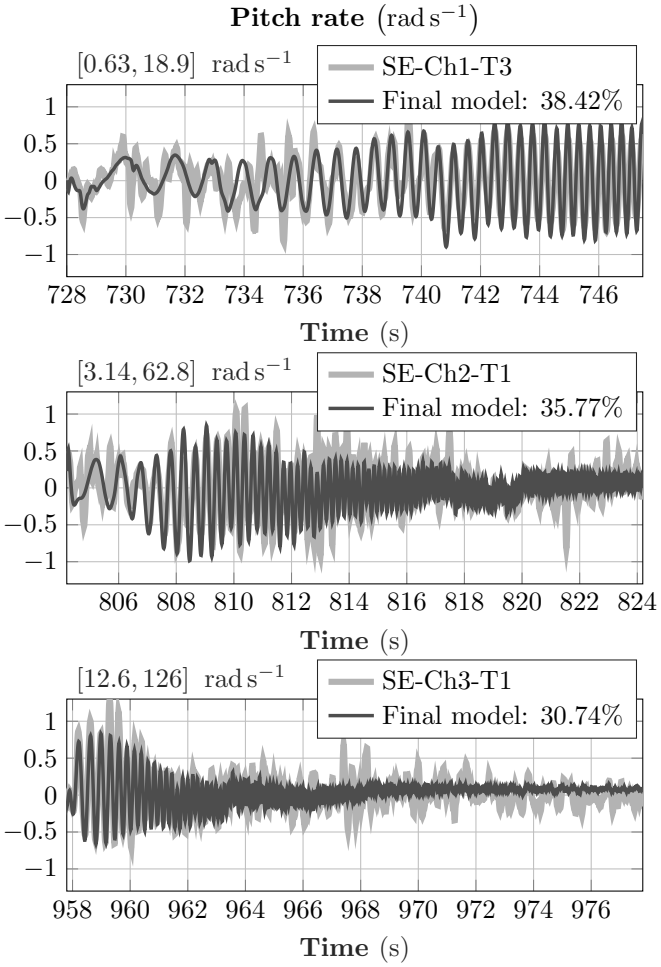

Fig. 9 Validation of the longitudinal aircraft model.

Although the fit percents achieved with the validation data set are only between 30% and 40%, it is more useful to evaluate the performance of the model over the frequency range of interest. In this regard, note that the simulations agree well with the experiments when the elevator chirp frequency is around the natural frequency of the short period mode, i.e. 17 rad s^{-1}. This occurs in the top subplot over the interval $[740, 748]$ s, in the middle subplot over the interval $[807, 810]$ s, and in the bottom subplot over the interval $[958, 960]$ s. On the other hand, the performance of the model is poor at very low frequencies (e.g. in the top subplot over the interval $[728, 736]$ s) because the phugoid mode and other low frequency dynamics are not characterized from the experiments. Similarly, the performance of the model is poor at very high frequencies (e.g. in the bottom subplot over the interval $[966, 978]$ s) because the model does not account for the exogenous disturbances that affect the experiment, such as atmospheric turbulence and sensor noise. Overall, the performance of the model is adequate around the natural frequency of the short period mode.

B. Lateral-Directional Model Validation

Time-domain simulations of the final model are compared against the roll rate responses recorded during the experiments SA-Ch1-T1, SA-Ch2-T2, SA-Ch3-T1. This selection includes one trial each from the low, the medium, and the high frequency ranges. None of these experiments are selected during the identification. Figure 10 shows the results of the validation over three subplots. The aileron chirp commands span the low (top subplot), the medium (middle subplot), and the high (bottom subplot) frequency ranges. In each subplot, the legend indicates the corresponding fit percent achieved by the final model. The plots indicate that the fit percents progressively decrease from the low to the high frequency ranges. Compared to the longitudinal model, the fit percents achieved with the lateral-directional model are higher for the low and the medium frequency range chirp commands.

As before, it is more useful to evaluate the performance of the model over the frequency range of interest. In this regard, note that the simulations agree well with the experiments when the aileron chirp frequency is around the natural frequency of the dutch roll mode, i.e. 4.8 rad s^{-1}. This occurs in the top subplot over the interval $[625, 632]$ s and in the middle subplot over the interval $[812, 818]$ s. The dutch roll mode is not excited in the bottom subplot. The simulations also agree well with the experiments at low frequencies, especially when compared with the longitudinal model. On the other hand, the performance of the model is poor at very high frequencies (e.g. in the bottom subplot over the interval $[918, 922]$ s) because the model does not account for the exogenous disturbances that affect the experiment, such as atmospheric turbulence and sensor noise. Overall, the performance of the model is adequate around the frequency of the dutch roll mode. The validated models are used to design, implement, and test feedback controllers. Additional details about the control design and the flight test results under closed-loop control can be found in [23].

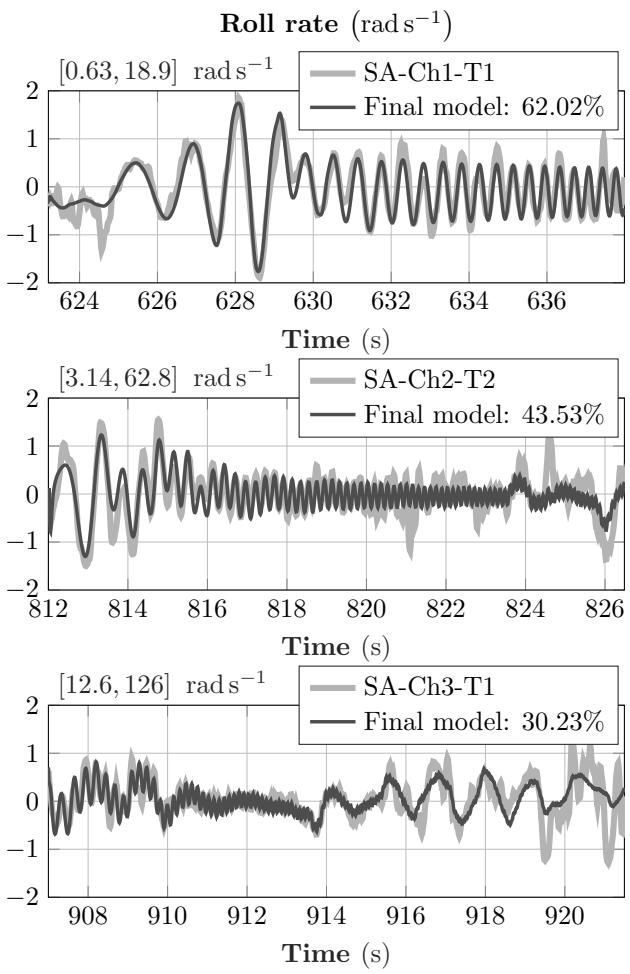

Fig. 10 Validation of the lateral-directional aircraft model.

V. Conclusions

This paper considers the system identification of a small, rudderless, fixed-wing unmanned aircraft. The flight dynamics of the aircraft is first modeled using physics-based first principles. In particular, the vortex lattice method (VLM) is used to estimate the aerodynamic stability and control derivatives. Flight tests are conducted to update the model parameters. The experiments reveal that the longitudinal dynamics predicted by VLM are sufficiently accurate in the frequency range desired for control design. On the other hand, the lateral-directional dynamics predicted by VLM differ from the experimental observations. Thus the lateral-directional stability and control derivatives are updated using the flight data. Additional flight tests reveal that the updated model parameters accurately capture the flight dynamics in the frequency range of interest for control design.

Funding Sources

This work was supported by the National Science Foundation under Grant No. NSF/CNS-1329390 entitled "CPS: Breakthrough: Collaborative Research: Managing Uncertainty in the Design of Safety-Critical Aviation Systems". The first author acknowledges financial support from the University of Minnesota through the 2017-2018 Doctoral Dissertation Fellowship.

Acknowledgments

The authors thank the following individuals: T. Colten of Sentera for donating the Vireo aircraft; C. Olson for the flight software, excitation signal implementation, and piloting; and N. Carter, R. Condron, L. Heide, A. Mahon, C. Regan, and B. Taylor for the aircraft integration and testing.

References

[1] Cook, M. V., *Flight Dynamics Principles*, 2nd ed., Elsevier, 2007, Chaps. 4, 5, 6, 7. doi:10.1016/B978-0-7506-6927-6.X5000-4.

[2] Nelson, R. C., *Flight Stability and Automatic Control*, McGraw-Hill, 1998, Chaps. 3, 4, 5, 6.

[3] Ljung, L., *System Identification: Theory for the User*, Prentice Hall PTR, 1999, Chaps. 3, 6, 7, 10, 13, 16.

[4] Soderstrom, T., and Stoica, P., *System Identification*, Prentice-Hall, 2001, Chaps. 3, 5, 6, 7.

[5] Tischler, M., and Remple, R., *Aircraft and Rotorcraft System Identification*, American Institute of Aeronautics and Astronautics, 2012, Chaps. 1, 2, 5, 6, 7. doi:10.2514/4.868207.

[6] Klein, V., and Morelli, E. A., *Aircraft System Identification: Theory And Practice*, American Institute of Aeronautics and Astronautics, 2006, Chaps. 4, 5.

[7] Jategaonkar, R. V., *Flight Vehicle System Identification: A Time-Domain Methodology*, American Institute of Aeronautics and Astronautics, 2006, Chaps. 4, 5, 6. doi:10.2514/4.866852.

[8] Morelli, E. A., "Low-Order Equivalent System Identification for the Tu-144LL Supersonic Transport Aircraft," *Journal of Guidance, Control, and Dynamics*, Vol. 26, No. 2, 2003, pp. 354–362. doi:10.2514/2.5053.

[9] Morelli, E. A., and Smith, M. S., "Real-Time Dynamic Modeling: Data Information Requirements and Flight-Test Results," *Journal of Aircraft*, Vol. 46, No. 6, 2009, pp. 1894–1905. doi:10.2514/1.40764.

[10] Bachelder, E., Thompson, P., Klyde, D., and Alvarez, D., "A New System Identification Method Using Short Duration Flight Test Inputs," *AIAA Atmospheric Flight Mechanics Conference*, 2011. doi:10.2514/6.2011-6445, AIAA Paper 2011-6445.

[11] Mettler, B., Tischler, M. B., and Kanade, T., "System identification modeling of a small-scale unmanned rotorcraft for flight control design," *Journal of the American Helicopter Society*, Vol. 47, No. 1, 2002, pp. 50–63. doi:10.4050/JAHS.47.50.

[12] Theodore, C. R., Tischler, M. B., and Colbourne, J. D., "Rapid Frequency-Domain Modeling Methods for Unmanned Aerial Vehicle Flight Control Applications," *Journal of Aircraft*, Vol. 41, No. 4, 2004, pp. 735–743. doi:10.2514/1.4671.

[13] Rohlf, D., Schmidt, S., and Irving, J., "Stability and Control Analysis for an Unmanned Aircraft Configuration Using System-Identification Techniques," *Journal of Aircraft*, Vol. 49, No. 6, 2012, pp. 1597–1609. doi:10.2514/1.C031392.

[14] Dorobantu, A., Murch, A., Mettler, B., and Balas, G., "System Identification for Small, Low-Cost, Fixed-Wing Unmanned Aircraft," *Journal of Aircraft*, Vol. 50, No. 4, 2013, pp. 1117–1130. doi:10.2514/1.C032065.

[15] Pfifer, H., and Danowsky, B. P., "System Identification of a Small Flexible Aircraft," *AIAA Atmospheric Flight Mechanics Conference*, 2016. doi:10.2514/6.2016-1750, AIAA Paper 2016-1750.

[16] Hale, L. E., Patil, M., and Roy, C. J., "Aerodynamic Parameter Identification and Uncertainty Quantification for Small Unmanned Aircraft," *Journal of Guidance, Control, and Dynamics*, Vol. 40, No. 3, 2017, pp. 680–691. doi:10.2514/1.G000582.

[17] Gremillion, G., and Humbert, J., "System Identification of a Quadrotor Micro Air Vehicle," *AIAA Atmospheric Flight Mechanics Conference*, 2010. doi:10.2514/6.2010-7644, AIAA Paper 2010-7644.

[18] Ljung, L., "System Identification Toolbox: Users Guide," Tech. rep., The MathWorks Inc., 2017.

[19] Mitikiri, Y., and Mohseni, K., "Modelling and Control of a miniature, low-aspect-ratio, fixed-delta-wing, rudderless aircraft," *AIAA Guidance, Navigation, and Control Conference*, 2018. doi:10.2514/6.2018-0876, AIAA Paper 2018-0876.

[20] Liu, M., Egan, G., and Ge, Y., "Identification of Attitude Flight Dynamics for An Unconventional UAV," *IEEE/RSJ International Conference on Intelligent Robots and Systems*, 2006, pp. 3243–3248. doi:10.1109/IROS.2006.282431.

[21] Liu, M., Egan, G. K., and Santoso, F., "Modeling, Autopilot Design, and Field Tuning of a UAV With Minimum Control Surfaces," *IEEE Transactions on Control Systems Technology*, Vol. 23, No. 6, 2015, pp. 2353–2360. doi:10.1109/TCST.2015.2398316.

[22] Flanagan, H. P., Hagerott, S. G., and Chao, H., "Model Based Roll Controller Tuning and Analysis for Small UAS in Turbulent Environments," *International Conference on Unmanned Aircraft Systems*, 2018, pp. 1398–1407. doi:10.1109/ICUAS.2018.8453442.

[23] Venkataraman, R., "Fault-Tolerant Flight Control Using One Aerodynamic Control Surface," Ph.D. thesis, University of Minnesota, 2018.

[24] Drela, M., and Youngren, H., "Athena Vortex Lattice," `web.mit.edu/drela/Public/web/avl`, 2017.